Journal of The Electrochemical Society, **166** (13) C421-C427 (2019)
0013-4651/2019/166(13)/C421/7/$38.00 © The Electrochemical Society

Theoretical Analysis of the Galvanic Corrosion Behavior of Mg-Ge Binary Alloy

Zhe Luo,[1,2] Jialiang Xu,[3] Yaowei Wang,[3] Tian Xie,[1] Hong Zhu,[3,4,z] Tao Ying,[1] Dejiang Li,[1] Leyun Wang,[1] Xiaoqin Zeng,[1,z] Chris Wolverton,[2] and Wenjiang Ding[1]

[1]*National Engineering Research Center of Light Alloy Net Forming, Shanghai Jiao Tong University, Shanghai 200240, China*
[2]*Department of Materials Science and Engineering, Northwestern University, Illinois 60208, USA*
[3]*University of Michigan - Shanghai Jiao Tong University Joint Institute, Shanghai Jiao Tong University, 200240, Shanghai, China*
[4]*The State Key Lab of Metal Matrix Composites, Shanghai Jiao Tong University, 200240, Shanghai, China*

A semi-empirical model based on the mixed potential theory and first principles calculation is developed in this study to analyze the galvanic corrosion of the Mg-Ge alloys composed of Mg and Mg_2Ge. The thermodynamic driving force of the Mg matrix dissolution is much stronger than that of the Mg_2Ge second phase, and Mg_2Ge will serve as the local cathode during the galvanic corrosion. The combination of the large anode equilibrium potential difference between Mg and Mg_2Ge, and the Schottky barrier across the interface indicates that the Mg_2Ge second phase can prevent the Mg grain from serving as the cathode and impede the electron transfer between the Mg grains. First principles calculations on the kinetics of hydrogen evolution reaction upon Mg_2Ge reveal that the rate-determining step is the hydrogen adsorption, which is extremely energetically unfavored but an inevitable intermediate state. The estimated exchange current density of the hydrogen evolution upon Mg_2Ge is about 3 orders of magnitude smaller than that on pure Mg. The depressed galvanic corrosion of the Mg-Ge alloys is the simultaneous result of the low hydrogen exchange current upon Mg_2Ge and preventing the Mg grains from serving as cathodes by the Mg_2Ge second phase. The calculated corrosion potentials of the Mg-Ge alloys in our model agree with the experimental values and our model can be used to guide the design of the corrosion-resistant Mg alloys.
 [DOI: 10.1149/2.1061913jes]

Manuscript submitted June 12, 2019; revised manuscript received August 22, 2019. Published August 30, 2019.

Mg alloys are considered as the lightest structural materials with high specific strengths,[1–4] and also the promising implant materials with excellent biocompatibilities.[5–7] However, the poor corrosion resistance of Mg alloys in solutions limits their applications.[3,8–10] Although coating is regarded as one of the most effective ways to prevent the corrosion of many materials,[11,12] the stress corrosion cracking (SCC) in Mg alloys cannot be prevented and may even be accelerated by coating.[12–15] This is because the anodic dissolution and the hydrogen embrittlement are considered as two of the main mechanisms of SCC,[16,17] and both the intrinsic dissolution of Mg and the hydrogen evolution in Mg alloys are fast due to the galvanic corrosion.[13] Moreover, the hydrogen bubbles and pits generated during the galvanic corrosion are also reported to accelerate the failure of the coating films.[18] So, it is very important to depress the dissolution and hydrogen evolution of Mg alloys themselves, namely, to improve the intrinsic corrosion resistance of Mg alloys.

Many experimental researches have been done to improve the intrinsic corrosion resistance of Mg alloys.[19–22] Since Mg is active and likely to form galvanic dipoles with the other phases in the alloys, Mg alloys suffer from strong galvanic corrosion.[23,24] In experiments, the galvanic corrosion is characterized by the polarization curves,[25] from which the extracted corrosion potential and current are frequently used to quantify the corrosion behaviors of alloys.[25,26] However, the discovery of new corrosion-resistant Mg alloys appears challenging, which may benefit from theoretical investigations and modeling of the corrosion behavior of Mg alloys. Given the importance of the polarization curves in galvanic corrosion, some theoretical efforts have been made to predict the galvanic corrosion behavior of Mg alloys from known thermodynamic and kinetic data.[27–30] Tayler developed a model for the galvanic corrosion of pure Mg based on first principles calculations, which agrees well with the experimental polarization curves of pure Mg.[27] The influence of solute atoms on the anodic dissolution of Mg matrix has been investigated by Ma[28] et al. and Luo[29] et al. respectively, while the cathodic reaction upon Mg and the influence of solute atoms on the hydrogen evolutions have been studied by Sumer.[30] However, the prediction of polarization curves of multiphase Mg alloys is rarely reported based on our best knowledge.

[z]E-mail: hong.zhu@sjtu.edu.cn; xqzeng@sjtu.edu.cn

In this study, we developed a model to analyze the galvanic corrosion behavior of multiphase alloys from thermodynamics and kinetics with the help of first principles calculations, based on which the polarization curves, corrosion potential and corrosion current density can be achieved. Recently, the Mg-0.3wt%Ge binary alloy composed of Mg matrix and Mg_2Ge second phase[21,31] was reported to be corrosion-resistant,[21] and the superior corrosion resistance was ascribed to the successful cathodic control due to the depressed hydrogen evolutions upon Mg_2Ge. Thus, Mg-Ge alloys are chosen as an ideal model system to start with to predict the galvanic corrosion behavior of multiphase alloys in a theoretical manner.

Modeling

In the polarization curves, the applied current density or the difference between anode and cathode current divided by the whole electrode area, i_{apply}, is plotted versus the potential E. In the mixed potential theory, i_{apply} versus E follows a similar formula to the Butler-Volmer equation, which can be further separated into the anode and cathode Tafel equations for E far from E_{corr} as shown in Figure 1a.[16] For a given electrode, the potential at which the reactant(s) and product(s) are in the thermodynamic equilibrium is noted as the electrode equilibrium potential E°, and the corresponding exchange current density is i°. The Tafel equation for anode (cathode) can be written as:

$$E - E^\circ_{a(c)} = \beta_{a(c)} \left(\log \left(i_{a(c)} \right) \right) - \log \left(i^\circ_{a(c)} \right)) \quad [1]$$

where $i_{a(c)}$ is current density at a given potential E, $i_{a(c)}$ is the anode (cathode) exchange current density, $E_{a(c)}$ is the anode (cathode) equilibrium potential, $\beta_{a(c)}$ is the Tafel slope and can be calculated by:[16]

$$\beta_{a(c)} = \frac{2.303 k_B T}{\alpha^{a(c)} n^{a(c)} e} \quad [2]$$

where $\alpha^{a(c)}$ and $n^{a(c)}$ are symmetry coefficient of charge transfer in the electrical double layer and transferred charge, respectively. T is the temperature, k_B is the Boltzmann constant, and e is the charge of one electron.

The mixed potential theory defines the corrosion potential E_{corr} as the electrode potential, at which the anodic, cathodic, and corrosion current are the same.[16,32] In other words, (E_{corr}, i_{corr}) is the solution of the equation set composed of the anodic and cathodic Tafel equations

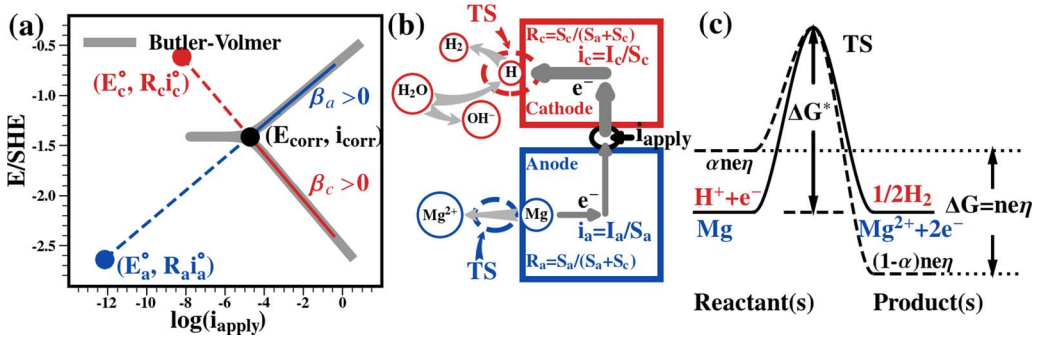

Figure 1. (a) Butler-Volmer equation can be separated into the anode (blue) and cathode (and) Tafel equation when the potential deviates far from E_{corr}. (b) In Mg alloys, Mg matrix usually serves as anode (blue rectangle), with a reaction of $Mg \rightarrow Mg^{2+} + 2e^-$; while the other phases serve as cathodes (red rectangle), the reaction upon which is hydrogen evolution. Applied current density in polarization curves, $i_{apply} = |R_a i_a - R_c i_c|$, is the difference between anode and cathode current divided by the whole electrode area. Electrode potential $E_{a(c)}$ in the Tafel equation is the equilibrium potential where the chemical potential of reactant(s) and product(s) are equal. Exchange current density $i_{a(c)}$ is limited by the reaction barrier, namely the energy difference between transition state (labeled as TS) and reactant(s) at $E_{a(c)}$. The Tafel slope $\beta_{a(c)}$ is characterized by the influence of overpotential $\eta_{a(c)} = E - E_{a(c)}$ on the reaction barrier as shown by (c). (c) η will make the chemical potential of reactants and products unequal and further lead to a change in energy barrier ΔG^*.

given by Eq. 1. This original mixed potential theory ignores the influence of electrode area, which is reported to be important.[16,33] Here we take into the account the influence of electrode area and extend the mixed potential theory as followed. If the anode area over the whole electrode area is called the anode area ratio, R_a (R_c is the cathode area ratio), E_{corr} and i_{corr} (corrosion current normalized by the total electrode area) can be calculated by:

$$E_{corr} = \frac{\beta_a E_c^\circ - \beta_c E_a^\circ}{\beta_a - \beta_c} + \frac{\beta_a \beta_c \left(\log\left(R_a^0 i_a^\circ\right) - \log\left(R_c^0 i_c^\circ\right)\right)}{\beta_a - \beta_c} \quad [3]$$

$$\log\left(i_{corr}\right) = \frac{E_c^\circ - E_a^\circ}{\beta_a - \beta_c} + \frac{\beta_a \log\left(R_a^0 i_a^\circ\right) - \beta_c \log\left(R_c^0 i_c^\circ\right)}{\beta_a - \beta_c} \quad [4]$$

Derivations of Eqs. 3 and 4 are provided in Appendix SI. Usually, Eq. 1 is fitted from the experimentally measured polarization curves at large electrode overpotential far from the corrosion potential.[25] To predict the polarization curves from scratch, we need to obtain the $E_{a(c)}$, $i_{a(c)}$, $\beta_{a(c)}$, and then rationally approximate R_a and R_c as shown in Figure 1.

During the corrosion of Mg, the cathode reaction is hydrogen evolution.[3] In experiments, the partial pressure of H_2 is usually set at 1 atm,[21] which implies that E_c^0, the cathode equilibrium potential, can be calculated by Nernst Equation: $E_c^\circ = -0.059$ pH(V/SHE).[34,35] The anode reaction of Mg alloys is the dissolution of Mg matrix or intermetallics into the solution or their oxidation by water. From thermodynamics, Mg or intermetallics will finally degrade into the equilibrium species at (pH, −0.059pH) in the Pourbaix diagrams, which are the anode reaction products. In addition to the experimental Pourbaix diagram, calculated ones by Persson et al.[36] can also be used to determine the anode reaction products. Then average anode potential of the overall degradation process, E_a° can also be calculated by Nernst equation based on the anode reaction. Chemical potential of the intermetallics were calculated based on the method proposed by Persson et al.[36] and the formation energies of the intermetallics were obtained from Open Quantum Materials Database (OQMD).[37] Two kinds of solutions where the anode reactions take place are considered: 1) the neutral solution free from common elements in Mg alloys,[38] where the ion concentration of products is set as low as 10^{-8} mol/L; 2) the saturated $Mg(OH)_2$ solution to include the influence of fast dissolution of Mg on the solution,[23,24] while the concentration of other ion products is still as low as 10^{-8} mol/L. Discussion on the choice of solutions can be found in the Appendix SII.

The exchange current density $i_{a(c)}^\circ$ and the Tafel slope $\beta_{a(c)}$ can be estimated by the kinetics on the electrodes.[28,39,40] In the case of pure Mg, both the anode and cathode kinetics have been reported.[28,35] We approximate the anode exchange current density of Mg, i_c° (Mg), with that upon the (0001) surface of Mg in Ma's result based on first principles calculations,[28] since Mg(0001) is the most energetically favored surface.[41] The anode Tafel slope of Mg, β_c(Mg), is fitted from experiments.[28,42] The cathode exchange current density i_c°(Mg) and the Tafel slope β_c(Mg) are approximated with the value of the high purity Mg at the open circuit condition from the experiments.[35] In the case of Mg_2Ge, we found that only i_c° and β_c are necessary (see section Validation of anode potential) but have not been reported yet. β_c can be calculated by Eq. 2 with parameters from the rate-determining step during hydrogen evolution,[43,44] where α^c is usually approximated as 0.5[16,27,28]. i_c° is reported to strongly depend on the adsorption free energy of H atom, ΔG_H, upon both metal and semiconductor electrodes, regardless of the pH of the solution.[39,45–47] This is because the hydrogen adsorption is an inevitable intermediate state during the hydrogen evolution as shown in Figure 1b, which is usually called the Volmer reaction. In the near neutral or base solutions, the Volmer reaction is given by:

$$H_2O + e^- \rightarrow *H + OH^- \quad [5]$$

where $*H$ is the adsorption state of H. Based on Nørskov,[39] when the cathode overpotential is $\eta^c = E - E_c^\circ$, the Volmer reaction energy, ΔG^c, is related to ΔG_H by:

$$\Delta G^c = \Delta G_H + e\eta. \quad [6]$$

Details about the definition of adsorption free energy and derivation of Eq. 6 are provided in Appendix SIII. Eq. 6 shows that a larger ΔG_H indicates a less energetically favored intermediate state of H adsorption. Given the significance of ΔG_H, Nøskov et al. fitted the exchange current density of hydrogen evolution in acid solution with the adsorption free energy of hydrogen.[39] Based on this method, we fitted the exchange current density in base solution[45] (closer to the solution where the polarization curves of the Mg alloys are usually measured) with hydrogen adsorption free energy[39] as shown in Figure S1, and estimated i_c° of Mg_2Ge with its hydrogen adsorption free energy. Influence of the screening effect on the electrical fields by the double layer on the reaction energy for Eq. 6 is neglected here, since it is small according to the results from Rossmeisl et al.[48]

The adsorption free energies were calculated based on density functional theory (DFT) implemented in the Vienna Ab initial Simulation Package (VASP)[49] with the Perdew-Burke-Ernzerhof (PBE) generalized gradient approximation (GGA)[50] and the projected augmented-wave (PAW)[51] pseudopotentials. The reaction barriers were calculated with the Nudged Elastic Band (NEB) method.[52] Calculation details are provided in Appendix SIV. Calculated lattice constant of Mg_2Ge is 4.54 Å, which is in good agreement with the experimental value 4.52 Å[53]. The adsorption energy and energy barriers were calculated on a 2 × 2 surface unit cell with (111) Mg^I termination of Mg_2Ge, which

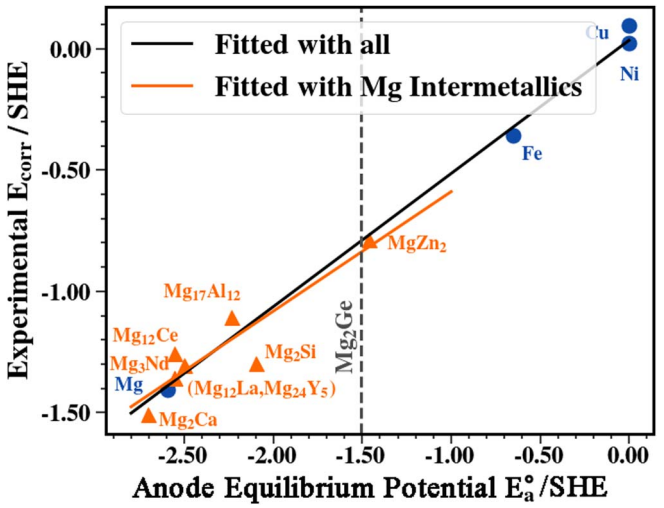

Figure 2. Calculated anode equilibrium potentials E_a° and experimental corrosion potentials E_{corr} of the common intermetallics and trace impurities in Mg alloys.[38] Elements and intermetallics are labeled as blue dots and orange triangles respectively and the triangle for $Mg_{12}La$ almost overlapped with that for $Mg_{24}Y_5$. The black line represents the relation fitted with the corrosion potentials and anode potentials of all the materials in the figure, while orange line fitted with Mg intermetallics only. The dashed vertical line represents the anode potential of Mg_2Ge.

is the lowest energy surface among all low index terminations considered in our study as shown in Figure S2 and Table S3, as well as the most stable termination observed in experiment.[54] Various adsorption sites with a coverage of adsorbate of 1/4 can be found in Figure S3–4.

The corrosion current density i_{corr} can be considered as a function of the anode and cathode electrode area ratios: $i_{corr} = i_{corr}(R_a, R_c)$. For binary phase alloys like Mg-Ge alloy, if all the Mg grains serve as the anode, the anode area ratio R_a can be approximated by the volume fraction of the Mg matrix, while R_c is approximated by the volume fraction of Mg_2Ge. In the pure Mg case, where both the anode and cathode are served by Mg, the worst case corresponding to the maximum corrosion current density is of most interest, because any increase of corrosion current density introduced by perturbations should be irreversible and the maximum i_{corr} may be reached with sufficient perturbations. As a result, in pure Mg, $R_a(\mathrm{Mg})$ and $R_c(\mathrm{Mg})$ are the electrode area ratio that maximizes the corrosion current density, in which $R_a(\mathrm{Mg}) + R_c(\mathrm{Mg}) = 1$. In Mg-Ge alloys, the possibility for Mg matrix to serve as both the anode and the cathode is discussed in Section Validation of anode potential and Anode and cathode area ratio. Detailed descriptions of electrode area ratio can be found in Appendix SV and Section Impact of Ge concentration.

Results

Validation of anode potential.—In experiments, the corrosion potential measurements are the simplest and most common way to quantify the difference in nobility and activity of materials, and a higher corrosion potential generally implies a higher nobility.[26] Here, we propose that the equilibrium potential E_a° of a material could be used to evaluate its thermodynamic driving force of dissolution. In Fig. 2, we plotted E_a° of the intermetallics and the trace impurities in the Mg alloys in the neutral and saturated $Mg(OH)_2$ solutions along with the experimental corrosion potential E_{corr} which were measured systematically in the same solution with the same equilibrium by Südholz[38] in Fig. 2 and Figure S3, respectively. E_a° versus experimental E_{corr} of the Al intermetallics and other elements in the neutral solution are shown in in Figure S5.[26,38,55,56] The degraded products in the different solutions are all listed in Table S5.

Actually, such a good positive linear relation between E_{corr} and E_a° in Figure 2 and S3 is not surprising and can be seen from Eq. 3, E_a° can be successfully applied to analyze the nobility of materials in the solutions. However, deviations from the fitted line may occur if the $\beta_{a(c)}$ and $\log(i_a^\circ) - \log(i_c^\circ)$ vary among different intermetallics. Compared with the well-known relation between E_{corr} and the Volta potential (work function),[55,57] E_a° derived from thermodynamics involves neither measurements nor complex surface calculations but could be used to estimate experimental E_{corr}. E_a° of Mg_2Ge is 1.08 V higher than E_a° of Mg. Thus the electrons should be "pushed" from Mg to Mg_2Ge and Mg_2Ge will serve as the local cathode. So only the cathode kinetics of hydrogen evolution upon Mg_2Ge are considered. However, the anisotropy of E_{corr} has not been considered here. For example, Jin et al. found that the anisotropy of Mg_2Si can lead to large difference in the measured corrosion potential with different terminations.[57] However, E_{corr} of Mg_2Si fitted from the model still lies in the range of experimental corrosion potentials of Mg_2Si.[26]

Cathode kinetics upon Mg_2Ge.—The hydrogen evolution reaction in the neutral or base solution can be separated into several step reactions as shown in Figure 3: (1) the water molecules adsorb on the surface; (2) the water molecular adsorbates dissociate into the H and OH adsorbates;[70] (3) the H adsorbates remain and the OH adsorbate consumes an electron and leaves as OH^- (the Volmer reaction); (4) the H adsorbates diffuse on the surface; (4) two nearby H adsorbates combine and release H_2 gas (the Tafel mechanism).[71] The hydrogen ion concentration in solutions is small and thus we ignore the Heyrovsky

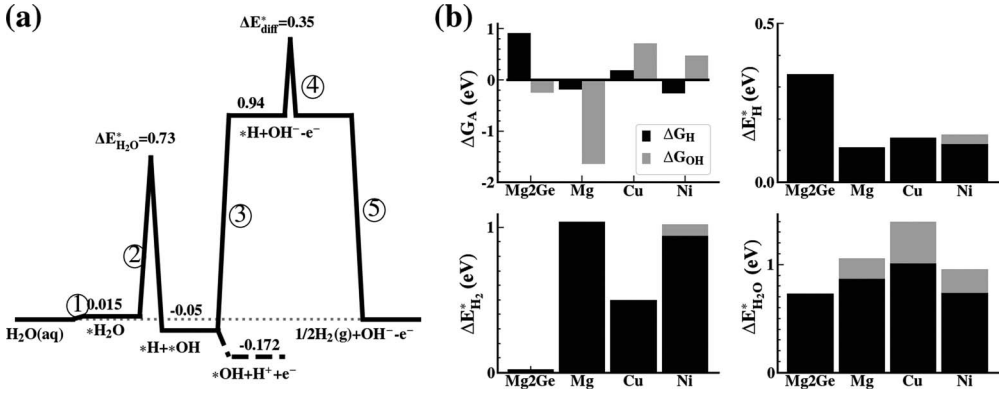

Figure 3. Reaction path and energy barrier (eV) of hydrogen evolution on the most stable surface of Mg_2Ge, (111)Mg1 at equilibrium potential for hydrogen evolution. The species at left (right) end are the reactants (products) of the hydrogen evolution in near neutral or base solution. The free energy of reactant and products are the same without overpotential, as shown by the horizontal dotted gray line. Comparison between the water dissociation barriers $\Delta E_{H2O}{}^*$, hydrogen diffusion barriers on the surface $\Delta E_H{}^*$, and hydrogen combination barriers $\Delta E_{H_2}{}^*$, adsorption free energy of H (ΔG_H) on Mg_2Ge, Mg, Cu and Ni are summarized from literature.[58–69] Grey bars in barriers represent the difference from various references.

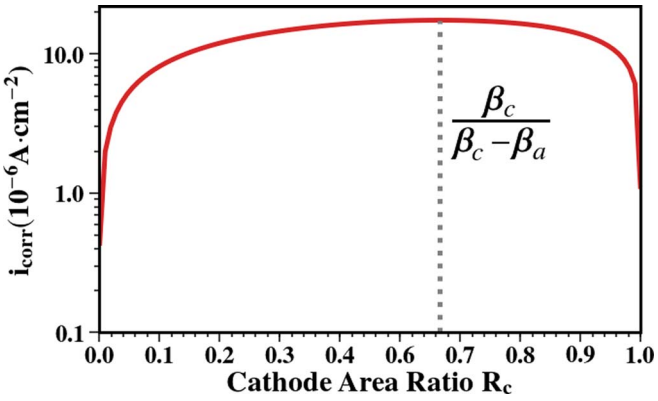

Figure 4. The corrosion current density of pure Mg as a function of the cathode area ratio R_c, under the constraint that the sum of anode and cathode area ratio is 1. The theoretical cathode area ratio maximizing the corrosion current of pure Mg is $\beta_c/(\beta_c-\beta_a)$.

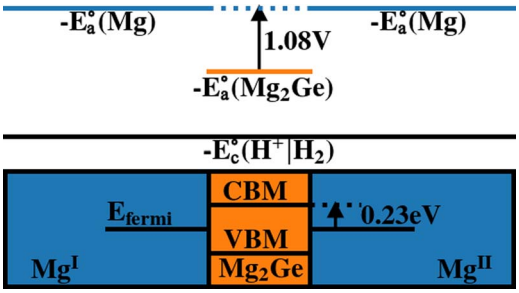

Figure 5. The potential profile in the Mg-Ge alloys. The anode equilibrium potential of Mg is 1.08 eV lower than that of Mg_2Ge. When Mg grains Mg^I and Mg^{II} are separated by Mg_2Ge, Schottky barrier (conduction band minimum, CBM, of Mg_2Ge with respect to the Fermi level of Mg, E_{fermi}) will hinder the electron transfer from Mg to Mg_2Ge as well as the electron transfer between Mg grains. The valence band maximum of Mg_2Ge is represented as VBM.

mechanism for the hydrogen gas evolution, in which the hydrogen adsorbate combines with the hydrogen ion in the solution and consumes an electron to form hydrogen gas. The important adsorption energy and step reaction barriers for Mg_2Ge, Mg, Cu and Ni are summarized in Figure 3. The detailed adsorption free energy is listed in Table S4, S6 and S7, and the adsorption sites are shown in Figure S3, S6, while the NEB calculation results of the water dissociation, hydrogen diffusion and hydrogen combination are shown in Figure S7–9.

The maximum energy barrier in the reaction path is the hydrogen adsorption. So the cathode Tafel slope on Mg_2Ge is approximated as 120 mV/decade according to Eq. 2.[43,44] As shown in Figure 3b, the adsorption energy of OH on Mg (0001) is negative, which indicates the OH adsorption is thermodynamically favored on the Mg(0001) surface, even if at a large negative overpotential. Thus, the Mg (0001) surface tends to be oxidized by water. Unlike Mg, the Mg_2Ge (111) Mg^I surface will not be oxidized during the galvanic corrosion in the common overpotential range of Mg alloys[23] (see in Figure S4). Based on the correlation between the exchange current density and the adsorption free energy of H on the clean metal surface as shown in Figure S1, and the computed ΔG_H on Mg_2Ge, we here estimated the cathode exchange current density i_c° on Mg_2Ge to be 1.65×10^{-11} A/cm^2, about 3 orders of magnitude smaller than that on Mg,[35] 5 orders of magnitude smaller than that on Cu,[45] one of the common trace impurities in Mg alloys.

Apart from the adsorption energy, other reaction barriers are also important. The water dissociation barrier upon Mg_2Ge is smaller than those on Cu (111), Ni (111) and Mg (0001).[27,60,66] If all the H adsorbates come from the water dissociation, the maximum hydrogen evolution velocity can be approximated by the H adsorbates generation velocity under the assumption that all the surface reaction sites are used for the water dissociation to generate the hydrogen adsorbates. However, the reported hydrogen exchange current densities from experiments are much larger than the predicted ones as shown in Figure S10. So for those with large water dissociation barriers, the H adsorbate may come from other sources, e.g., the direct adsorption of H^+, whereas the reaction energy of direct H^+ adsorption is the same as Eq. 5 as shown in the Appendix SIII. However, the diffusion barrier of H adsorbs upon Mg_2Ge is also larger than that on Mg (0001), Cu (111) and Ni (111),[61–64,66] which should make the Tafel mechanism more difficult. The combination barrier of H_2 upon Mg_2Ge is much smaller than that on Mg (0001), Cu (111) and Ni (111),[67–69] which may derive from the fact that the H adsorbs are strongly energetically unfavored with a large ΔG_H.

Anode and cathode area ratio.—The calculated i_{corr} of pure Mg as a function of cathode area ratio is plotted in Figure 4 under the constraint that the sum of cathode and anode area ratio is 1. For the galvanic corrosion of pure Mg, the solution is set as the saturated $Mg(OH)_2$ solution to represent the pH of the local solutions due to the fast dissolution of Mg during the steady state corrosion. The R_c maximizing the corrosion is $\beta_c/(\beta_c-\beta_a)$ as shown in Figure 4, which can be derived from Eq. 4. The calculated corrosion current density is about 1.5×10^{-5} A/cm^2, which is close to the experimental value.[72] This maximum i_{corr} can be reached with sufficient perturbations to push R_c to $\beta_c/(\beta_c-\beta_a)$, which in pure metal, comes from the heterogeneous nature of metal surface (e.g. various crystal faces, grain boundaries, defects).[16] However, when the perturbation is not strong enough, e.g., the grains are large and grain boundaries area ratio is small, it is hard for the adjustment of cathode and anode area ratio, and the corrosion current cannot reach the maximum value. So, from this point of view, larger grain size may be accompanied with smaller perturbations and hence a smaller corrosion current, which is consistent with experimental observations for pure Mg.[73–75]

In multiphase Mg alloys, the large difference in the anode equilibrium potential between Mg matrix and the other phases may serve as the strong perturbation for the galvanic corrosion. However, when the surface area of the other phases is small, it is still probable that the Mg matrix is able to serve as the cathode to compensate for the low cathode current limited by the area of the other phases and thus accelerate the overall corrosion rate. On the other hand, the existence of the second phase between Mg grains may defer the electron transfer between Mg grains given the electrical resistivity of second phase and interface. It is found that SiC particles in Al alloys can improve their corrosion resistance because the SiC/Al interface can trap and stabilize the electrons, indicating the possibility of interface engineering to improve corrosion resistance.[76] In the case of the Mg-Ge alloys, the Mg_2Ge second phase was reported to distribute along the grain boundaries[21] or at the interdendritic areas,[77] which indicates that Mg_2Ge separates the Mg grains. If two Mg grains, Mg^I and Mg^{II} are separated by Mg_2Ge, the corresponding potential profile is shown in Figure 5. The anode equilibrium potential difference between Mg and Mg_2Ge, is 1.08 V, much greater than the potential difference from the heterogeneous nature of pure Mg, e.g, the work function difference (about 0.1 eV) between common surfaces.[41] As a consequence, all the electrons will be pushed from Mg^I and Mg^{II} to Mg_2Ge in solution. Moreover, as a semiconductor, Mg_2Ge has a higher specific electrical resistance while its bandgap may also result in a Schottky barrier across the interface hindering the electron transfer between Mg grains. To calculate this barrier, we built an interface model between Mg (0001) and Mg_2Ge (111)Mg^I, both of which are the most energetically favored surfaces.[41,54] It is found that the bandgap of Mg_2Ge (n-type under Mg rich condition[78]) does lead to a Schottky barrier of 0.23 eV at the interface, hindering the electron transfer as shown in Figure 5. Details about band alignments and interface calculations can be found in Figure S11.[79,80] The barrier height is also larger than the aforementioned work function difference between various surfaces of pure Mg. As a result, this Schottky barrier will defer the electron transfer from Mg to Mg_2Ge, as well as between Mg grains.

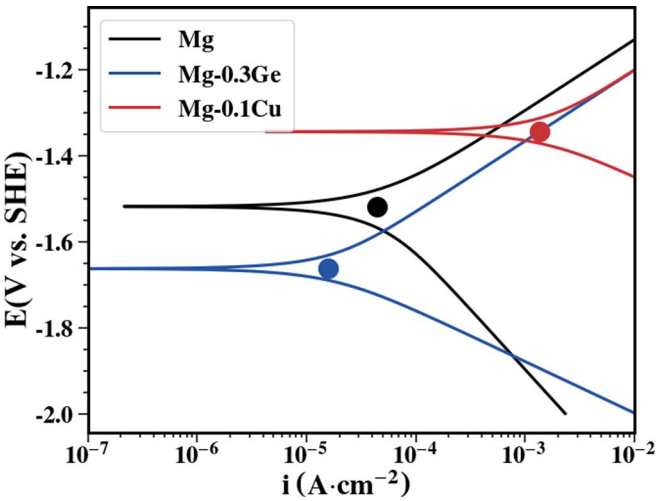

Figure 6. Predicted polarization curves of pure Mg, Mg-0.3wt%Ge (labeled as Mg-0.3Ge) and Mg-0.1wt%Cu (labeled as Mg-0.1Cu) in saturate $Mg(OH)_2$ solution. The solid circles represent the corrosion current density and potential. For Mg-Ge and Mg-Cu alloys, all the Mg grains are considered as anode, while all the second phase as cathode. Solubility of Ge and Cu is taken into account when determining the volume of second phase. β_c of Cu is approximated as 120 mV/decade, i_c° of Cu is from Reference 45.

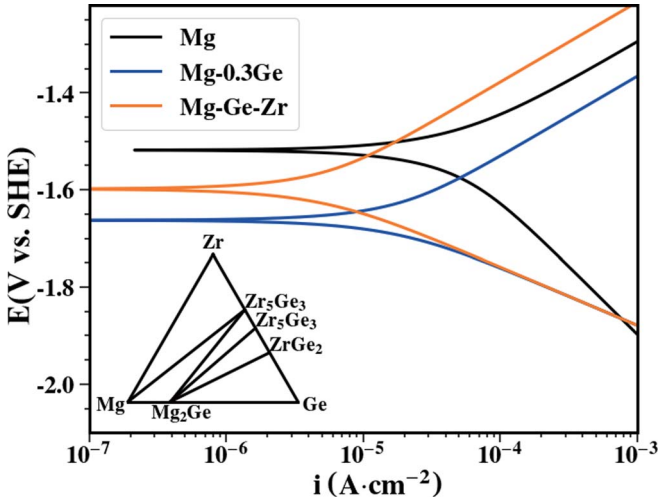

Figure 7. The predicted polarization curve of Mg-Zr-0.3Ge alloy compared to those of Mg-0.3Ge alloy and pure Mg, if Mg-Zr-0.3Ge is still composed of Mg and Mg_2Ge with Zr near grain boundaries of Mg. The calculated Mg-Ge-Zr ternary phase diagram by DFT[81,82] indicates that Zr_5Ge_3 phase needs to be avoided during synthesis.

Thus, if the Mg grains are completely separated by the Mg_2Ge, the charge transfer between the Mg grains not only suffers from the overwhelming thermodynamic driving force difference of dissolution between Mg and Mg_2Ge, but also the Schottky barrier near the interface of Mg and Mg_2Ge. When the volume of the Mg_2Ge is large enough and separates all the Mg grains from each other, the cathode area ratio R^c can be approximated by the volume fraction of the Mg_2Ge in the Mg-Ge alloys and similar for R^a. However, when the volume of the Mg_2Ge is too small to separate all the Mg grains apart, though the Mg_2Ge is still local cathode, the Mg grains directly connected with the other Mg grains can also serve as the cathode to maximize the corrosion current. If 1 volume of the Mg_2Ge can separate v_f volumes of the Mg grains apart and prevent them from being cathodes, the area ratio of Mg serving as cathode among those Mg grains connected with the other Mg grains is determined by the method described in Appendix SV. If we assume that the volume fraction of the Mg_2Ge in the Mg-0.3Ge (0.3 wt% Ge) alloy is exactly the one which can separate all Mg grains apart, v_f is about 340 from phase diagram.[31] However, v_f may still vary in different alloy systems under different synthesis conductions. Detailed modeling of v_f can be found in Appendix SVI and discussion about situations where v_f is other than 340 can be found later.

Predicted polarization curves.—The predicted polarization curves for pure Mg, the Mg-0.3Ge and the Mg-0.1Cu alloys from the electrode potentials, exchange current densities and Tafel slopes calculated in the previous sections are shown in Figure 6. We applied the method proposed by Luo[29] and find that solute Ge's influence of the anodic behavior of Mg matrix is negligible. In addition, there is no solubility of Ge in the Mg matrix. As a result, the anodic exchange current density on Mg matrix in Mg-Ge alloys is approximated to be the same as that in pure Mg. In the Mg-0.3Ge alloy, all the Mg_2Ge serves as cathode and the Mg grains are assumed to be anode. The predicted polarization curves and corrosion potential E_{corr} and corrosion current density i_{corr}, in principle, could be compared with experiments directly.

The corrosion potential E_{corr} of the Mg-0.3Ge alloys calculated in our model with $\beta_c(Mg) = 230$mV/decade is 0.14 V lower than that of pure Mg, while the corrosion current density i_{corr} of Mg-0.3Ge is about only one third of that of pure Mg. If the cathode Tafel slope β_c of Mg is set as 120 mV/decades as Ma et al. did,[28] the addition of 0.3wt% of Ge will decrease the E_{corr} by 0.4 V compared with pure Mg, while the i_{corr} is depressed by 2 orders of magnitude. The decrease of both E_{corr} and i_{corr} is caused by the depressed cathodic kinetics as shown in Figure 6. The anodic current of Mg-0.3Ge is larger than that of pure Mg due to the increased anode area ratio of Mg, because some of the Mg grains will serve as the cathode in pure Mg as discussed in Section 3.3. Using the similar approaches, we plotted the polarization curve of the Mg-0.1Cu alloy in Figure. 6, considering that the trace impurity limit of Cu in Mg matrix is 0.1wt% Cu. In our model, the addition of 0.1wt% Cu increases i_{corr} by 30 times, which is consistent with experimental observation that the addition of Cu greatly accelerates the galvanic corrosion.[8] However, the anodic branch of the Mg-0.1Cu polarization curve lies to the right of pure Mg, and almost overlaps with that of the Mg-0.3Ge, which implies that the kinetics of hydrogen evolution upon Cu with 0.1 wt% is fast enough that all the Mg grains serve as anode.

Discussion

Application of the model.—The success of our model implies that it can be used to guide the design of the corrosion-resistant Mg alloys combined with DFT calculations. For example, according to our analysis, the slow cathodic kinetics upon Mg_2Ge comes from: (1) the large hydrogen adsorption energy; (2) the existence of bandgap and a large Schottky barrier preventing the electron transfer between Mg grains; (3) a proper anode potential difference that pushes electrons from Mg to the second phase. These reasons indicate that second phase candidates to improve the corrosion resistance of Mg alloys may be found among semiconductor or insulating materials with large hydrogen adsorption energies and proper anode potentials. Apart from the cathode reaction, the influence of solute atoms on the anode reaction of Mg matrix can also be taken into account. Although solubility of Ge in Mg is 0 and we ignored its influence on the anode reaction, the solubility of Zr in Mg is 2.69 wt%.[83] Experiments indicate that Zr can stabilize the Mg atoms on the surface,[19] while Luo predicted by DFT calculations that anode local potential of Zr-doped Mg (0001) surface is 0.15 V higher than pure Mg. In a hypothetical Mg-Ge-Zr ternary alloy, if the solute Zr atoms distribute on the surface of Mg and Mg_2Ge functions the same as that in Mg-Ge binary alloys, the polarization curves of the Mg-Zr-Ge ternary alloy should be similar to that shown in Figure 7. Not only the corrosion potential of Mg-Zr-0.3Ge alloy is raised by 0.06V compared to Mg-0.3Ge, but the corrosion current density can be further depressed to only 1/4 of that of Mg-0.3Ge. However, the calculated Mg-Zr-Ge phase diagram tells us that

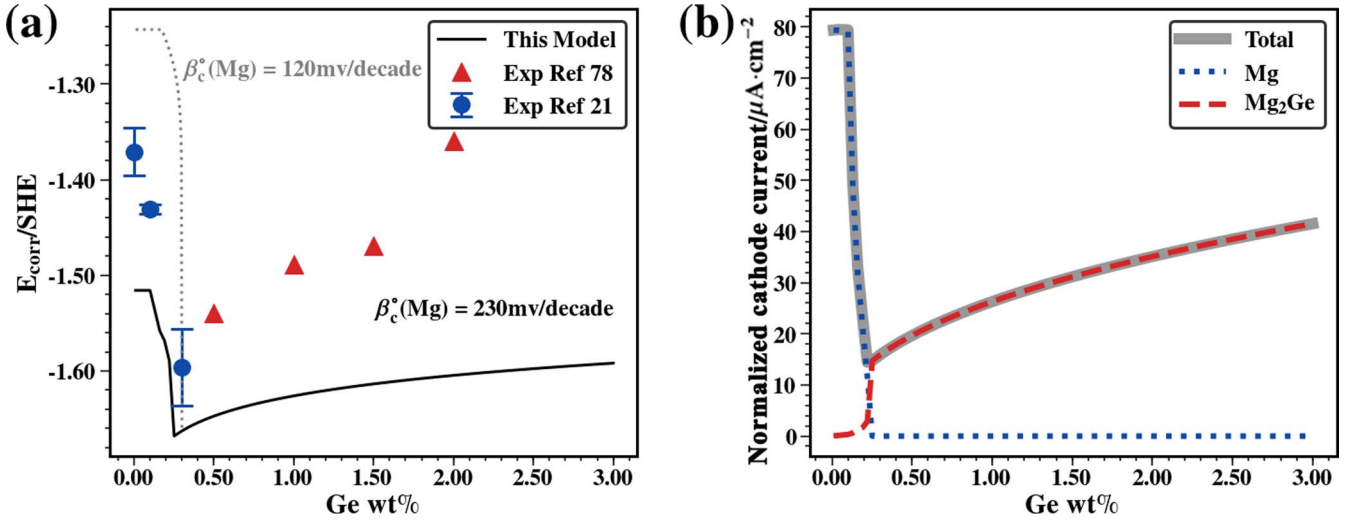

Figure 8. (a) Corrosion potential and (b) normalized cathode current (cathode current divided by the total electrode area, $i_{a(c)} \times R_{a(c)}$) at corrosion potential with different Ge concentration under the approximation that 1 volume of Mg_2Ge can hinder 340 volumes of Mg grains from being cathode. The experimental values represented by blue solid circles is estimated from Reference 21, while those by red triangles is from Reference 77. Two different cathode Tafel slopes of Mg, 120 mV/decade in Ma's modeling[28] and 280 mV/decade from experiments[35] are used. The normalized cathode current upon Mg and Mg_2Ge are separated, while the sum of two normalized cathode currents represented by solid gray line with extra weight should be the corrosion current density.

the content of Zr must also be small enough to avoid the appearance of Zr_5Ge_3 phase to make Zr solute in Mg as much as possible. Recently, a Mg-Ge-Zn dilute ternary alloy was also reported to have good corrosion resistance,[84] which could also explained by the same reason as the Mg-Ge-Zr systems proposed here.

Impact of Ge concentration.—Given that the solubility of Ge in Mg is 0[83], the Ge addition will only introduce the Mg_2Ge second phase, which leads to a larger cathode area ratio and may also separate Mg grains and prevent Mg from being cathode as discussed in Section Anode and cathode area ratio. The corrosion potential E_{corr} is plotted in Figure 8, which is close to the experimental measurements. The change of E_{corr} and i_{corr} with the increase of the Ge concentration can be separated into 2 parts: a sharp drop due to a decrease of normalized cathode current upon Mg over all electrode area, and a slow rise due to the increase of the Mg_2Ge cathode area. As discussed in Section Anode and cathode area ratio, when the concentration of Ge increases from 0 to 3 wt%, the Mg grains are gradually separated by the Mg_2Ge second phase, and less Mg grains are able to serve as cathode, which leads to the fast drop of the normalized cathodic current upon Mg as shown by the blue dashed lines in Figure 8b. Meanwhile, normalized cathode current upon the Mg_2Ge increases exponentially with the Ge concentration due to the combination of a larger cathodic overpotential and an increase of cathode area, whereas it is still small given the slow kinetics for the hydrogen evolution upon Mg_2Ge as shown in Section Cathode kinetics upon Mg_2Ge. As a consequence, the reduction in the normalized cathode current shifts the cathodic branch in Figure 6 downward, accompanied with a simultaneous reduction in E_{corr} and i_{corr}. When the Mg grains are all separated by the Mg_2Ge, corrosion current upon Mg is 0, and that upon Mg_2Ge rises gently with the increase of Ge addition due to a larger area ratio of Mg_2Ge.

Figure 8 is plotted under the approximation that 1 volume of the Mg_2Ge in the alloy can prevent 340 volumes of Mg grains from being cathodes ($v_f = 340$). However, it is expected that v_f may change under different synthesis conditions. If v_f is less than 340, the decrease of the normalized cathode current upon the Mg is less sharp, which leads to a larger minimum corrosion current density introduced by Ge and vice versa as shown in Figure S12, where the corrosion current density versus Ge wt% is plotted for v_f is 100, 340 and 500 respectively.

Thus, the depressed corrosion potential comes from the combination of the slow kinetics of hydrogen evolution upon Mg_2Ge and the prohibition of Mg serving as cathode by Mg_2Ge. If the hydrogen evolution upon second phase is too fast, e.g., Cu, the corrosion current density will still be large, as shown in Figure 6. On the other hand, if Mg_2Ge tends to segregate and fails to separate Mg grains, more Mg grains will be able to serve as cathode. As a result, the drop of the normalized cathode current upon Mg with the addition of Mg_2Ge second phase will be slower.

Limitation of the model.—Our model is still semi-empirical, in which some of the parameters in the Tafel equation is obtained directly from experiments or fitted with experimental data. Further first principles calculations and modeling are necessary to make a pure ab initio prediction of the galvanic corrosion behavior, such as determining the charge transfer coefficient with DFT calculations as Skulason did,[40] a detailed analysis about the hydrogen evolution kinetics on pure Mg, and a comprehensive modeling that predicts the hydrogen exchange current density with data merely from first principles calculations. Passivation is also not considered in this model, while part of the influence can be taken into account by changing the total effective electrode areas by setting $R_a + R_c < 1$ under the approximation that neither anode and cathode reaction takes place upon passivated electrode. However, the hydrogen evolution upon $Mg(OH)_2$ is reported to be higher than Mg by Salleh,[85] and further investigation is necessary to take this into account.

Conclusions

In this study, we developed a semi-empirical model of galvanic corrosion based on the mixed potential theory and analyzed the galvanic corrosion behavior of Mg-Ge alloys. The following conclusions can be safely reached from our study:

(1) the anode equilibrium potential in our study can serve as a descriptor of the nobility of the intermetallic phases; in the Mg-Ge alloys, the maximum thermodynamic driving force for corrosion is the dissolution of the Mg matrix, and the Mg_2Ge serves as the local cathode;
(2) the large thermodynamic driving force difference of the dissolution of Mg and Mg_2Ge in the solutions, the microscopic distributions of Mg_2Ge in Mg-Ge alloy, and the Schottky barrier at the Mg/Mg_2Ge interface prevent electrons transfer between the Mg grains and hinder the Mg grains from serving as cathode;
(3) the hydrogen evolution upon Mg_2Ge is limited by the Volmer reaction, combined with a high H adsorption energy on the surface and a low surface coverage of H;

(4) the depressed galvanic corrosion is resulted from both the slow hydrogen kinetics on the local cathode Mg_2Ge, and prohibiting the Mg grains from being cathodes.

The trend of calculated corrosion potential from our model agrees well with the experiments and our model can be used to guide the design of the corrosion-resistant Mg alloys.

Acknowledgments

This work is supported by the National Key R&D Plan (2016YFB0301002), National Natural Science Foundation of China (51474149) and the research grant (No. 16DZ2260600) from Science and Technology Commission of Shanghai Municipality. CW acknowledges support under the financial assistance Award 70NANB14H012 from the US Department of Commerce, National Institute of Standards and Technology as part of the Center for Hierarchical Materials Design (CHiMaD).

ORCID

Hong Zhu https://orcid.org/0000-0001-7919-5661

References

1. B. L. Mordike and T. Ebert, *Mater Sci Eng A*, **302**, 37 (2001).
2. M. K. Kulekci, *Int J Adv Manuf Technol*, **39**, 851 (2008).
3. G. L. Song and A. Atrens, *Adv Eng Mater*, **1**, 11 (1999).
4. R. L. Edgar, *Magnes Alloy Their Appl*, 1–8 (2006).
5. J. Kim, H. M. Mousa, C. H. Park, and C. S. Kim, *Appl Surf Sci*, **396**, 249 (2017).
6. S. M. Kim, M. H. Kang, H. E. Kim, H. K. Lim, S. H. Byun, J. H. Lee, and S. M. Lee, *Mater Sci Eng C*, **81**, 97 (2017).
7. S. Virtanen, in *Mater. Sci. Eng. B Solid-State Mater. Adv. Technol.*, **176**, 1600 (2011).
8. G. Song and A. Atrens, *Adv Eng Mater*, **5**, 837 (2003).
9. F. Cao, G. L. Song, and A. Atrens, *Corrosion and passivation of magnesium alloys*, p. 835, (2016).
10. S. Agarwal, J. Curtin, B. Duffy, and S. Jaiswal, *Mater Sci Eng C*, **68**, 948 (2016).
11. J. E. Gray and B. Luan, *J Alloys Compd*, **336**, 88 (2002).
12. S. Jafari, S. E. Harandi, and R. K. Singh Raman, *Jom*, **67**, 1143 (2015).
13. N. Winzer, A. Atrens, G. Song, E. Ghali, W. Dietzel, K. U. Kainer, N. Hort, and C. Blawert, *Adv Eng Mater*, **7**, 659 (2005).
14. I. A. Levin, *Intercrystalline corrosion and corrosion of metals under stress*, Consultants bureau 1962., (1962).
15. V. B. Yakovlev, L. P. Trutneva, N. I. Isayev, and G. Nemetch, *Prot MetUSSR*, **20**, 300 (1984).
16. E. McCafferty, *Introduction to corrosion science*, Springer Science & Business Media, (2010).
17. F. Cao, Z. Shi, G. L. Song, M. Liu, M. S. Dargusch, and A. Atrens, *Corros Sci*, **96**, 121 (2015).
18. A. Srinivasan, K. S. Shin, and N. Rajendran, *RSC Adv*, **6**, 49910 (2016).
19. G. Song and D. StJohn, *J Light Met*, **2**, 1 (2002).
20. W. Xu, N. Birbilis, G. Sha, Y. Wang, J. E. Daniels, Y. Xiao, and M. Ferry, *Nat Mater*, **14**, 1229 (2015).
21. R. L. Liu, M. F. Hurley, A. Kvryan, G. Williams, J. R. Scully, and N. Birbilis, *Sci Rep*, **6**, 28747 (2016).
22. N. Birbilis, G. Williams, K. Gusieva, A. Samaniego, M. A. Gibson, and H. N. McMurray, *Electrochem Commun*, **34**, 295 (2013).
23. F. Cao, Z. Shi, G. L. Song, M. Liu, and A. Atrens, *Corros Sci*, **76**, 60 (2013).
24. Z. Shi, F. Cao, G. L. Song, M. Liu, and A. Atrens, *Corros Sci*, **76**, 98 (2013).
25. Z. Shi, M. Liu, and A. Atrens, *Corros Sci*, **52**, 579 (2010).
26. R. G. Buchheit, *J Electrochem Soc*, **142**, 3994 (1995).
27. C. D. Taylor, *J Electrochem Soc*, **163**, C602 (2016).
28. H. Ma, X. Q. Chen, R. Li, S. Wang, J. Dong, and W. Ke, *Acta Mater*, **130**, 137 (2017).
29. Z. Luo, H. Zhu, T. Ying, D. Li, and X. Zeng, *Surf Sci*, **672–673**, 68 (2018).
30. A. Sumer and S. Chaudhuri, *Corrosion*, **73**, 596 (2017).
31. A. A. Nayeb-Hashemi, J. B. Clark, R. W. Olesinski, and G. J. Abbaschian, *Bull Alloy Phase Diagr.*, **5**, 359 (1984).
32. C. W. Wagner and W. Traud, *Elektrochem*, **44**, 391 (1938).
33. D. R. Banjade, S. D. Porter, B. M. McMullan, and J. N. Harb, *J Electrochem Soc*, **163**, C116 (2016).
34. G. S. Frankel, A. Samaniego, and N. Birbilis, *Corros Sci*, **70**, 104 (2013).
35. S. Fajardo and G. S. Frankel, *Electrochim Acta*, **165**, 255 (2015).
36. K. A. Persson, B. Waldwick, P. Lazic, and G. Ceder, *Phys Rev B - Condens Matter Mater Phys*, **85**, 1 (2012).
37. J. E. Saal, S. Kirklin, M. Aykol, B. Meredig, and C. Wolverton, *Jom*, **65**, 1501 (2013).
38. A. D. Südholz, N. T. Kirkland, R. G. Bucheit, and N. Birbilis, *Electrochem Solid State Lett*, **14**, C5 (2011).
39. J. K. Nørskov, T. Bligaard, a. Logadottir, J. R. Kitchin, J. G. Chen, S. Pandelov, and U. Stimming, *J Electrochem Soc*, **152**, J23 (2005).
40. E. Skúlason and V. Tripkovic, *J Ldots*, 18182 (2010).
41. R. Tran, Z. Xu, D. W. Balachandran Radhakrishnan, W. Sun, K. A. Persson, and S. P. Ong, *Sci Data*, 3 (2016).
42. G. L. Song, *JOM*, **64**, 671 (2012).
43. S. Fletcher, *J Solid State Electrochem*, **13**, 537 (2009).
44. Y. Li, H. Wang, L. Xie, Y. Liang, G. Hong, and H. Dai, *J Am Chem Soc*, **133**, 7296 (2011).
45. W. Sheng, M. Myint, J. G. Chen, and Y. Yan, *Energy Env. Sci*, **6**, 1509 (2013).
46. Q. Tang and D. Jiang, *ACS Catal*, **6**, 4953 (2016).
47. J. Greeley, T. F. Jaramillo, J. Bonde, I. B. Chorkendorff, and J. K. Nørskov, *Nat Mater*, **5**, 909 (2006).
48. J. Rossmeisl, J. K. Nørskov, C. D. Taylor, M. J. Janik, and M. Neurock, *J Phys Chem B*, **110**, 21833 (2006).
49. G. Kresse and J. Hafner, *Phys Rev B*, **47**, 558 (1993).
50. J. P. Perdew, K. Burke, and M. Ernzerhof, *Phys Rev Lett*, **77**, 3865 (1996).
51. P. E. Blöchl, *Phys Rev B*, **50**, 17953 (1994).
52. G. Henkelman and H. Jónsson, *J Chem Phys*, **113**, 9978 (2000).
53. E. Zintl and H. Kaiser, *Z. Für Anorg Allg Chem.*, **211**, 113 (1933).
54. P. W. Li, S. N. Lee, and G. C. Danielson, *Phys Rev B*, **6**, 442 (1972).
55. M. F. Hurley, C. M. Efaw, P. H. Davis, J. R. Croteau, E. Graugnard, and N. Birbilis, *Corrosion*, **71**, 160 (2015).
56. N. Birbilis and R. G. Buchheit, *J Electrochem Soc*, **152**, B140 (2005).
57. Y. Jin, M. Liu, C. Zhang, C. Leygraf, L. Wen, and J. Pan, *J Electrochem Soc*, **164**, C465 (2017).
58. T. Jiang, L. X. Sun, and W. X. Li, *Phys Rev B - Condens Matter Mater Phys*, 81 (2010).
59. G. C. Wang, S. X. Tao, and X. H. Bu, *J Catal*, **244**, 10 (2006).
60. A. A. Phatak, W. N. Delgass, F. H. Ribeiro, and W. F. Schneider, *J Phys Chem C*, **113**, 7269 (2009).
61. M. Pozzo, G. Carlini, R. Rosei, and D. Alfè, *J Chem Phys*, **126**, 164706 (2007).
62. L. Kristinsdóttir and E. Skúlason, *Surf Sci*, **606**, 1400 (2012).
63. G. W. Watson, R. P. K. Wells, D. J. Willock, and G. J. Hutchings, *J Phys Chem B*, **105**, 4889 (2001).
64. G. Kresse and J. Hafner, *Surf Sci*, **459**, 287 (2000).
65. K. S. Williams, J. P. Labukas, V. Rodriguez-Santiago, and J. W. Andzelm, *Corrosion*, **71**, 209 (2015).
66. M. Pozzo, D. Alfe, A. Amieiro, S. French, and A. Pratt, *J Chem Phys*, **128**, 94703 (2008).
67. B. Hammer, M. Scheffler, K. W. Jacobsen, and J. K. Nørskov, *Phys Rev Lett*, **73**, 1400 (1994).
68. K. Nobuhara, H. Kasai, W. A. Diño, and H. Nakanishi, *Surf Sci*, **566–568**, 703 (2004).
69. C. Díaz, R. A. Olsen, H. F. Busnengo, and G. J. Kroes, *J Phys Chem C*, **114**, 11192 (2010).
70. B. You, X. Liu, G. Hu, S. Gul, J. Yano, D. E. Jiang, and Y. Sun, *J Am Chem Soc*, **139**, 12283 (2017).
71. Y. H. Fang, G. F. Wei, and Z. P. Liu, *J Phys Chem C*, **117**, 7669 (2013).
72. N. Birbilis, K. D. Ralston, S. Virtanen, H. L. Fraser, and C. H. J. Davies, *Corros Eng Sci Technol*, **45**, 224 (2010).
73. S. Gollapudi, *Corros Sci*, **62**, 90 (2012).
74. D. Song, A. B. Ma, J. Jiang, P. Lin, D. Yang, and J. Fan, *Corros Sci*, **52**, 481 (2010).
75. K. D. Ralston, N. Birbilis, and C. H. J. Davies, *Scr Mater*, **63**, 1201 (2010).
76. S. Mosleh-Shirazi, G. Hua, F. Akhlaghi, X. Yan, and D. Li, *Sci Rep*, **5**, 1 (2015).
77. B. Kim, K. Park, H. Kimura, Y. Park, and I. Park, *Mater. Trans.*, **53**, 240 (2012).
78. X. Liu, L. Xi, W. Qiu, J. Yang, T. Zhu, X. Zhao, and W. Zhang, *Adv Electron Mater*, **2**, 1500284 (2016).
79. R. T. Tung, *Phys Rev Lett*, **52**, 461 (1984).
80. B. Liu, L.-J. Wu, Y.-Q. Zhao, L.-Z. Wang, and M.-Q. Cai, *RSC Adv*, **6**, 60271 (2016).
81. A. Jain, S. P. Ong, G. Hautier, W. Chen, W. D. Richards, S. Dacek, S. Cholia, D. Gunter, D. Skinner, G. Ceder, and K. a. Persson, *APL Mater*, **1**, 11002 (2013).
82. S. P. Ong, L. Wang, B. Kang, and G. Ceder, *Chem Mater*, **20**, 1798 (2008).
83. K. Gusieva, C. H. J. Davies, J. R. Scully, and N. Birbilis, *Int Mater Rev*, **60**, 169 (2015).
84. R. Liu, Z. Zeng, J. Scully, G. Williams, and N. Birbilis, *Corros. Sci.* (2018).
85. S. H. Salleh, S. Thomas, J. A. Yuwono, K. Venkatesan, and N. Birbilis, *Electrochim Acta*, **161**, 144 (2015).